

A Hierarchical Image Matting Model for Blood Vessel Segmentation in Fundus Images

Zhun Fan, *Senior Member, IEEE*, Jiewei Lu, Caimin Wei,
Han Huang, Xinye Cai, Xinjian Chen*, *Senior Member, IEEE*,

Abstract—In this paper, a hierarchical image matting model is proposed to extract blood vessels from fundus images. More specifically, a hierarchical strategy is integrated into the image matting model for blood vessel segmentation. Normally the matting models require a user specified *trimap*, which separates the input image into three regions: the foreground, background and unknown regions. However, creating a user specified *trimap* is laborious for vessel segmentation tasks. In this paper, we propose a method that first generates *trimap* automatically by utilizing region features of blood vessels, then applies a hierarchical image matting model to extract the vessel pixels from the unknown regions. The proposed method has low calculation time and outperforms many other state-of-art supervised and unsupervised methods. It achieves a vessel segmentation accuracy of 96.0%, 95.7% and 95.1% in an average time of 10.72s, 15.74s and 50.71s on images from three publicly available fundus image datasets DRIVE, STARE, and CHASE_DB1, respectively.

Index Terms—Image matting, hierarchical strategy, fundus, *trimap*, region features, segmentation, vessel.

I. INTRODUCTION

RETINAL blood vessels generally show a coarse to fine centrifugal distribution and appear as a wire mesh-like structure or tree-like structure [1]. Their morphological features, such as length and width, is of great importance in the early detection and therapy of different angiocardopathy and ocular diseases such as stroke, vein occlusions, diabetes and arteriosclerosis [2]–[4]. The analysis of morphological features of retinal blood vessels is conducive to detecting and treating a disease in time when it is still in its early stage. Since angiocardopathy and ocular diseases have a serious impact on human's life, the analysis of retinal blood vessels is of great significance in many clinical applications to reveal important information of systemic diseases and support diagnosis and

treatment. As a result, the requirement of vessel analysis system grows rapidly, in which vessel segmentation is the first and one of the most crucial steps.

Vessel segmentation has become an important research field in recent years [5]. Broadly speaking, existing vessel segmentation approaches include two categories: supervised and unsupervised. In supervised methods, a number of different features are extracted from fundus images, and applied to train the effective classifiers with the purpose of extracting retinal blood vessels. In [6], Staal *et al.* extract 27 features for each image pixel with ridge profiles, and perform feature selection by using sequential forward selection method to choose the pixels that can generate better segmentation performance by a K-Nearest Neighbor classifier. Soares *et al.* [7] introduce a feature-based Bayesian classifier with Gaussian mixtures, which makes use of the intensity information and Gabor wavelet transform responses to build a 7-D feature vector for each pixel. In [8], Lupascu *et al.* train an AdaBoost classifier with 41 features which incorporates various structure and geometry information. Marin *et al.* [9] extract 7 features including intensity and geometry information, and then train a neural network classifier for vessel extraction. Roychowdhury *et al.* [10] extract the major vessel from the fundus images and use a Gaussian classifier for vessel segmentation with 8 features, which consists of intensity features and gradient features. Liskowski *et al.* [11] employ a deep neural network to extract vessel pixels from fundus images. Daniele *et al.* [12] use an U-Net [13] to achieve blood vessel segmentation. In unsupervised methods, the researchers try to discover latent vessel properties for vessel segmentation. Unsupervised methods can be further divided into multiscale approaches, matched filtering, vessel tracking, mathematical morphology and model based methods [5]. The multiscale approach introduced by [14] develops a vessel enhancement filter for vessel extraction with the analysis of image structure. The matched filtering method described by [15] employs different threshold probes to draw vessel pixels from the filtered images. The methodology based on vessel tracking [16] applies a wave propagation and traceback mechanism to label each pixel the likelihood of belonging to vessels in angiography images. The mathematical morphology with the extraction of vessel centerlines [17] is also developed to find the morphological characteristics of retinal blood vessels. Model based methods generally use geometric deformable models [18], parametric deformable models [19], vessel profile models [20] and active contour models [21] for blood vessel segmentation.

Image matting means precisely segmenting the foreground

Zhun Fan is a Full Professor with the School of Electrical and Information Engineering, Shantou University, Shan'tou 515063, China. Zhun Fan and Jiewei Lu are with the Guangdong Provincial Key Laboratory of Digital Signal and Image Processing, College of Engineering, Shantou University, Shan'tou 515063, China (email: zfan, ljwlu1@stu.edu.cn).

Caimin Wei is with the Department of Mathematics, Shantou University, Shan'tou 515063, China (email: cmwei@stu.edu.cn).

Han Huang is with the School of Software Engineering, South China University of Technology, Guang'zhou 510006, China (email: hhan@scut.edu.cn).

Xinye Cai is with the College of Computer Science and Technology, Nanjing University of Aeronautics and Astronautics, Jiang'su 210016, China (email:xinye@nuaa.edu.cn).

Xinjian Chen is a Distinguished Professor with the School of Electrical and Information Engineering, Soochow University, Suzhou, 215006, China. He is also with the State Key Laboratory of Radiation Medicine and Protection, Soochow University, Suzhou, 215123, China (email: xjchen@suda.edu.cn).

* indicates the corresponding author.

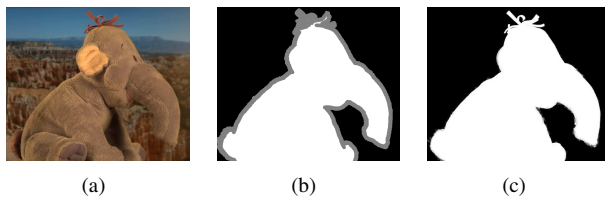


Fig. 1. The process of image matting. (a) An image. (b) A trimap generated by the user. The white, black and gray regions belong to the foreground, background and unknown regions, respectively. (c) A result achieved by [22].

from an image. Generally image matting includes two main steps. The first step is generating a user specified *trimap*. Fig.1(b) gives an example of a user specified trimap. Trimap is a hand-drawn segmented image, which is composed of the foreground, background and unknown regions. The second step is employing the matting model to pick the pixels belonging to the foreground from the unknown regions, on the basis of the samples of foreground and background pixels annotated by the observers. Fig.1(c) gives an exemplary result achieved by [22]. Image matting is of great importance in many applications, such as, image (or video) segmentation, video production, new view synthesis, and film making. To the best of our knowledge, image matting has rarely been employed previously to extract blood vessels from fundus image, and so far we have only found [23], which uses Hu’s moment features [9] and KNN matting [24] to perform blood vessel segmentation. The major reason is that generating a user specified trimap for vessel segmentation is an extremely laborious and time-consuming task. In other words, it is not appropriate to obtain a trimap manually for vessel segmentation. In addition, a proper image matting model needs to be designed carefully to improve the vessel segmentation performance. In order to address these issues, region features of blood vessels are employed to generate the trimap automatically. Then a hierarchical image matting model is proposed to draw the vessel pixels from the unknown regions. The proposed model is evaluated on the public available datasets DRIVE, STARE, and CHASE_DB1, which have been extensively used by other scientists to develop their own methods. The segmentation performance verifies the efficiency and effectiveness of the proposed hierarchical image matting model.

The remainder of this paper is constructed as follows: Section II introduces some background knowledge of image matting. Section III details the process of generating the trimap of a fundus image automatically, and the proposed hierarchical image matting model. Section IV introduces the public available datasets and the commonly used evaluation metrics. The experimental results are detailed in Section V. The conclusion is provided in Section VI.

II. IMAGE MATTING

As aforementioned, image matting aims to accurately extract the foreground given a trimap of an image. Concretely, the input image I can be considered as a linear aggregation of a foreground image F and a background image B :

$$I = \alpha_z F + (1 - \alpha_z) B \quad (1)$$

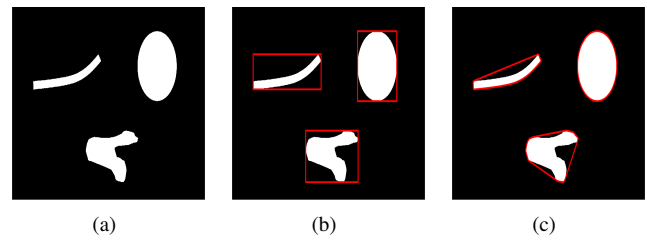


Fig. 2. An example to illustrate the bounding box and convex hull. (a) The exemplary image. (b) The image for the illustration of bounding box. The red boxes are the bounding boxes. (c) The image for the illustration of convex hull. The red polygons are the convex hulls.

where alpha matte α_z indicates the probability of the foreground, which ranges from 0 to 1.

After obtaining the user specified trimap, to derive the α_z in the unknown regions, Chuang *et al.* [25] uses sets of Gaussian distribution to obtain the color models of the foreground and background colors, and estimates the optimal alpha value by using a maximum-likelihood criterion. In [26], Levin *et al.* derives an effective objective function based on the color smooth hypothesis, and employs this function to obtain the optimum of the alpha matte. Zheng *et al.* [22] performs image matting based on the local and global learning methods. In [27], Kaiming *et al.* solves a large kernel matting Laplacian, and achieves a fast matting algorithm. In [28], Shahrian and Rajan use an effective cost function to select the optimal (F, B) couple for alpha matte evaluation. In [24], Qifeng *et al.* proposes a matting technique, and obtains an efficient result by leveraging on the preconditioned conjugate gradient method. Shahrian *et al.* [29] expands the sampling range of foreground and background regions, and collects a representative set of samples for image matting. In [30], Cho *et al.* presents an image matting method to assess alpha mattes on sub-images of a light field image. Karacan [31] *et al.* proposes a sampling method, and employs a new distance metric to obtain the results of image matting. In [32], Cho *et al.* utilizes a deep convolutional neural network to achieve image matting. Li *et al.* [33] designs a novel feature and three-layer graph framework for image matting. Aksoy *et al.* [34] designs an inter-pixel information flow to achieve image matting. In [35], Lee *et al.* performs parallel image matting on large images with multiple processing cores.

III. METHODOLOGY

In this section, the process of generating the trimap of an input fundus image automatically is introduced, followed by detailing the proposed hierarchical image matting model.

A. Trimap Generation

Region features of blood vessels have been used for blood vessel segmentation and performed well on segmentation accuracy and computational efficiency [36]. In this paper, the trimap of an input fundus image is generated automatically by utilizing region features of blood vessels. The definitions of regions features are given as follows:

- **Area** indicates the number of pixels in the region.

- **Bounding Box** specifies the smallest rectangle incorporating the region. Fig.2(b) gives an example of bounding box.
- **Extent** represents the region proportion in the bounding box.
- **VRatio** represents the ratio of the length to the width of the bounding box.
- **Convex Hull** means the smallest convex polygon incorporating the region. Fig.2(c) gives an example of convex hull.
- **Solidity** represents the region proportion in the convex hull.

TABLE I

THE DEFAULT THRESHOLD VALUES OF REGION FEATURES: *Extent*, *VRatio*, *Solidity* AND THEIR RECOMMENDED RANGES USED IN THIS WORK

Threshold values	e_1	e_2	r	s
Default values	0.35	0.25	2.2	0.53
Recommended Ranges	[0.2, 0.4]	[0.15, 0.3]	[2, 6]	[0.4, 0.6]

The default threshold values of region features: *Extent*, *VRatio*, *Solidity* and their recommended ranges used in this work are reported in Table I. e_1 and e_2 are two threshold values of *Extent* features used in this work; r is the threshold value of *VRatio* feature; s is the threshold value of *Solidity* feature. For *Area* feature, two threshold values: $a_1 = f_i \times 2$ and $a_2 = f_i \times 35$ are used in this work. f_i , called the internal factor, is calculated as $d \times \frac{\max(h,w)}{\min(h,w)}$, where $d = 21$ is roughly the diameter of the biggest vessels in fundus images [37], h and w are the height and width of the fundus image.

The proposed model is not sensitive to the above mentioned region features. In other words, these region features can be selected in a relatively large range without sacrificing the performance. In Section V(D)-"Sensitivity analysis of threshold values of region features and the weight parameter", empirical study is directed to demonstrate the insensitivity of the proposed model to the threshold values of region features.

Creating the trimap of the input fundus image automatically includes two main steps: 1) Image Segmentation and 2) Vessel Skeleton Extraction. The process of trimap generation is given in Fig.3.

1) *Image Segmentation*: Image segmentation aims to separate the input image into three regions: the vessel (foreground), background and unknown regions. Firstly the enhanced vessel image I_{mr} generated by morphological reconstruction [37] is segmented into three regions: the background regions (B), unknown regions (U) and preliminary vessel regions (V_1)

$$I_{mr} = \begin{cases} B & \text{if } 0 < I_{mr} < p_1 \\ U & \text{if } p_1 \leq I_{mr} < p_2 \\ V_1 & \text{if } p_2 \leq I_{mr} \end{cases} \quad (2)$$

where $p_1 = 0.2$ and $p_2 = 0.35$ restrict the unknown region as thin as possible in order to achieve the better matting result [28], [38]. In order to remove the noise regions in V_1 , the regions with $Area > a_1$ in V_1 are extracted firstly (V_1^*). Then regions in V_1^* whose $Extent \leq e_1$ && $VRatio \leq r$ && $Solidity \geq s$ are abandoned, resulting in the denoised preliminary vessel regions V_2 . Fig.4 gives an exemplary process of image segmentation.

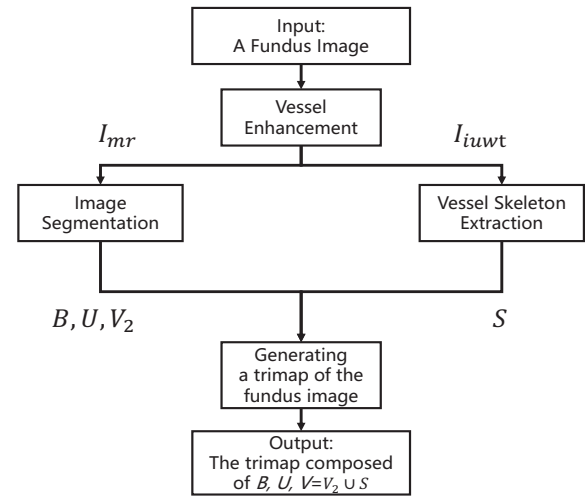


Fig. 3. The process of trimap generation. B represents the background regions; U represents the unknown regions; V_2 represents the denoised preliminary vessel regions; S represents the skeleton of blood vessels; V represents the vessel regions.

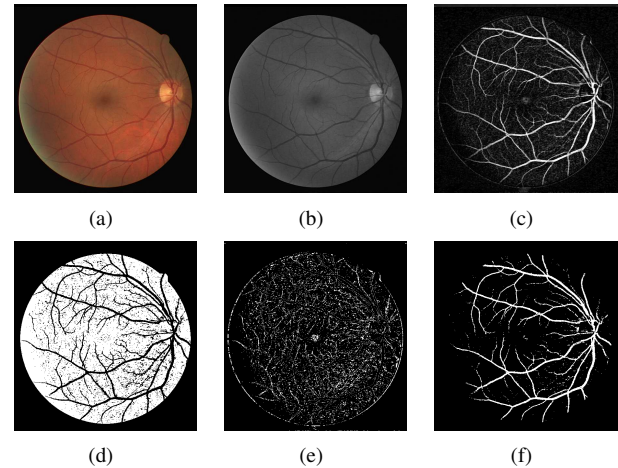


Fig. 4. Image segmentation. (a) The fundus image I . (b) The green plane of the fundus image I_g . (c) The enhanced vessel image I_{mr} . (d) The background regions B . (e) The unknown regions U . (f) The denoised preliminary vessel regions V_2

2) *Vessel Skeleton Extraction*: Vessel Skeleton Extraction aims to further distinguish the unknown regions and provide more information on blood vessels. In Section V(B)-"Vessel Segmentation Performance", the effectiveness of vessel skeleton extraction will be presented. Firstly, a segmented image T is generated by thresholding the enhanced vessel image I_{iuilt} generated by the isotropic undecimated wavelet transform [39].

$$T = \begin{cases} 1 & I_{iuilt} > t \\ 0 & I_{iuilt} \leq t \end{cases} \quad (3)$$

where $t = Otsu(I_{iuilt}) - \varepsilon$, ε is set as 0.03. Then T is divided into three regions according to the *Area* feature:

$$T = \begin{cases} T_1 & \text{if } 0 < Area < a_1 \\ T_2 & \text{if } a_1 \leq Area \leq a_2 \\ T_3 & \text{if } a_2 < Area \end{cases} \quad (4)$$

In vessel skeleton extraction, the regions in T_3 are preserved while the regions in T_1 are abandoned. Then the regions in

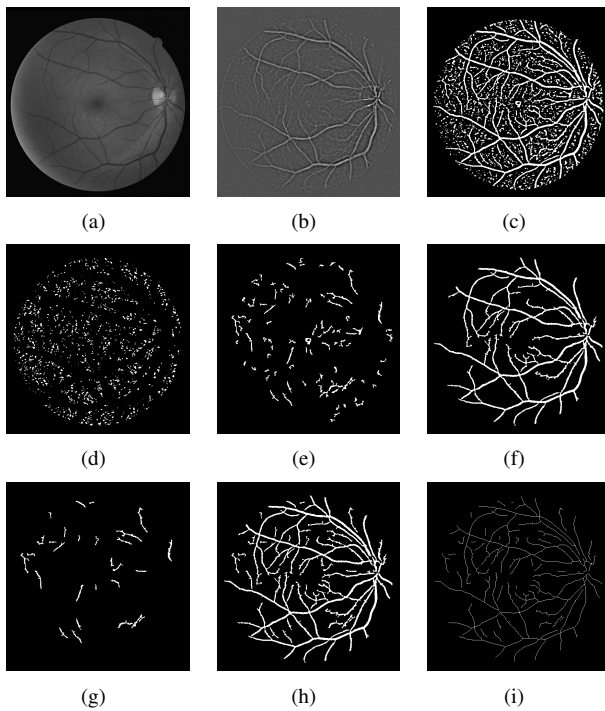


Fig. 5. Vessel skeleton extraction. (a) The green plane of the fundus image I_g . (b) The vessel enhanced image I_{iuv} . (c) The binary image T . (d) The background regions T_1 . (e) The candidate regions T_2 . (f) The vessel regions T_3 . (g) T_4 : The preserved regions in T_2 . (h) The combined regions of T_3 and T_4 . (i) The vessel skeletons S .

T_2 with $Extent > e_2$ && $VRatio \leq r$ are preserved as T_4 . Finally skeleton extraction [40] is performed on the combined regions of T_3 and T_4 in order to obtain the vessel skeleton S . Fig.5 gives an exemplary process of vessel skeleton extraction.

After performing image segmentation and vessel skeleton extraction, the trimap of the input fundus image is generated (as shown in Fig.6(b)), which is composed of the background regions (B), unknown regions (U) and vessel (or foreground) regions ($V = V_2 \cup S$).

B. Hierarchical Image Matting Model

Hierarchical image matting model is proposed to label the pixels in the unknown regions as vessels or background in an incremental way. Specifically, after stratifying the pixels in unknown regions (called unknown pixels) into m hierarchies by a hierarchical strategy, let u_i^j indicates the i th unknown pixel in the j th hierarchy, the segmented vessel image $I_v(u_i^j)$ is modeled as follows:

$$I_v(u_i^j) = \begin{cases} 1 & \text{if } \beta(u_i^j, V) > \beta(u_i^j, B) \\ 0 & \text{else} \end{cases} \quad (5)$$

where β indicates the correlation function (depicted in Equation (8)). The implementation of the hierarchical image matting model consists of two main steps:

Step 1 *Stratifying the unknown pixels*: Stratify pixels in the unknown regions into different hierarchies.

Step 2 *Hierarchical update*: Assign new labels (V or B) to pixels in each hierarchy.

The pseudocode implementing this model is shown in Algorithm 1.

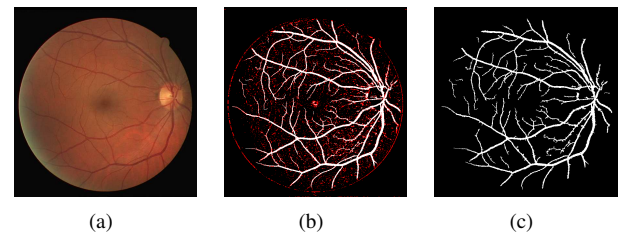


Fig. 6. (a) An input image. (b) A trimap generated by the proposed method. The white, black and red regions belong to the foreground, background and unknown regions, respectively. (c) The result achieved by the proposed hierarchical image matting model.

Algorithm 1: Implementing the hierarchical image matting model

Input: Trimap composed of B, U, V

Output: The segmented vessel image I_v

Step 1: Stratifying the unknown pixels:

- a) For $i = 1, \dots, n_U$, set $D(i) = d_i$, where n_U is the number of unknown pixels in U , d_i is the Euclidean distance between the i th unknown pixel and the closest vessel pixel in V , D is the set of d_i .
- b) Sort the unknown pixels in U in an ascending order according to the distances D , cluster the pixels with the same distance into one hierarchy, stratify the pixels into m hierarchies and denote them as an hierarchical order set: $H = \{H_1, H_2, \dots, H_m\}$, $H_j = \{u_i^j | i \in 1, 2, \dots, n_i\}$, where n_i is the number of unknown pixels in the j th hierarchy H_j .

Step 2: Hierarchical Update

For $j = 1, \dots, m$, do

For $i = 1, \dots, n_i$, do

- a) Compute the correlations (Defined in Equation (8)) between u_i^j and its neighboring labelled pixels (vessel pixels and background pixels) included in a 9×9 grid.
- b) Choose the labelled pixel with the closest correlation, and assign its label (V or B) to u_i^j .

end for

end for

Stratifying the unknown pixels: In this stage, the unknown pixels are stratified into different hierarchies. For the i th unknown pixel in U , its Euclidean distances with all vessel pixels in V are calculated first. Then the closest distance d_i is chosen and assigned to the i th unknown pixel. After that, the unknown pixels are stratified into different hierarchies according to the closest distances. The first hierarchy has the lowest value of the closest distance while the last hierarchy has the highest value of the closest distance. The unknown pixels reside in low hierarchy suggests that they are close to blood vessels; The unknown pixels stay in high hierarchy indicates that they are far away from blood vessels. Fig.7 gives an exemplary process of stratifying the unknown pixels.

Correlation Function: In step 2 of Algorithm 1, given an unknown pixel u_i^j and its neighboring labelled pixel k_l^j , a color cost function β_c is defined to describe the fitness of u_i^j and k_l^j first:

$$\beta_c(u_i^j, k_l^j) = \|c_{u_i^j} - c_{k_l^j}\| \quad (6)$$

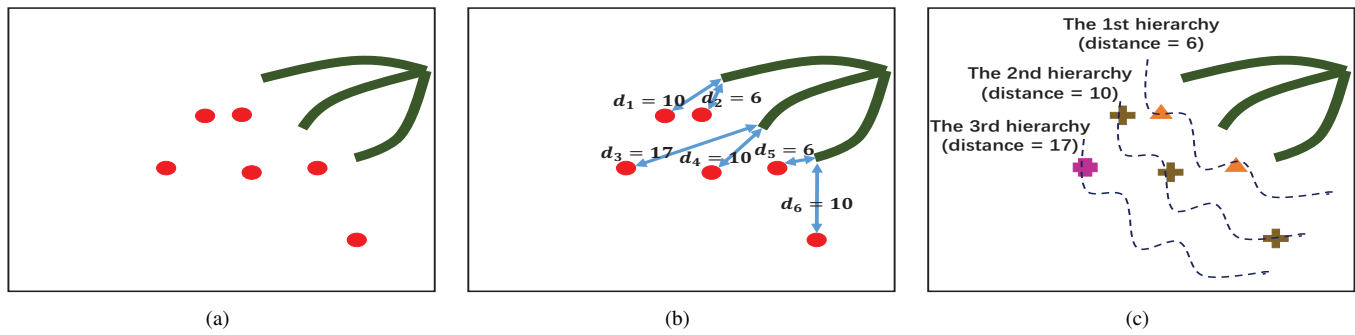


Fig. 7. An exemplary process of stratifying the unknown pixels. (a) An exemplary image (green pixels represent vessel pixels, red pixels represent unknown pixels). (b) Calculating the closest distance for each unknown pixel (d_i means the closest distance for the i th unknown pixel). (c) Stratifying unknown pixels into different hierarchies.

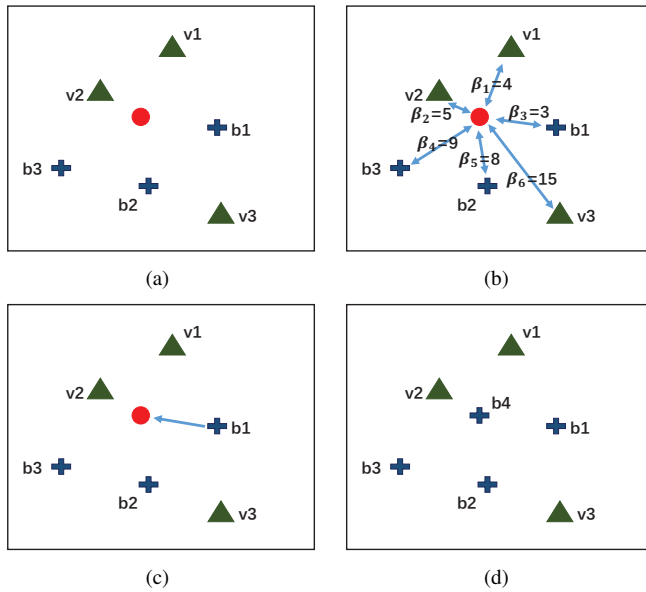


Fig. 8. An example for the illustration of assigning a label (V or B) to an unknown pixel. (a) An exemplary image (green triangles represent vessel pixels, blue pluses represent background pixels, red points represent unknown pixels). v_i indicates the i th vessel pixel, b_i indicates the i th background pixel. (b) Calculating the correlation functions between an unknown pixel and its neighboring labelled pixels (vessel pixels and background pixels) (β_i means the correlation between the unknown pixel and the i th labelled pixel). (c) Assigning a label (V or B) to the unknown pixel. (d) The resultant image.

where $c_{u_i^j}$ and $c_{k_l^j}$ are intensity level of u_i^j and k_l^j in I_{mr} . A spatial cost function β_s is further defined:

$$\beta_s(u_i^j, k_l^j) = \frac{\|x_{u_i^j} - x_{k_l^j}\| - x_{min}}{x_{max} - x_{min}} \quad (7)$$

where $x_{u_i^j}$ and $x_{k_l^j}$ are the spatial coordinates of u_i^j and k_l^j . The terms $x_{max} = \max_j \|x_{u_i^j} - x_{k_l^j}\|$ and $x_{min} = \min_j \|x_{u_i^j} - x_{k_l^j}\|$ are the maximum and minimum distance of the unknown pixel u_i^j to the labelled pixel k_l^j . The normalization factors x_{min} and x_{max} ensure that β_s is independent from the absolute distance.

Our final correlation function β is a combination of the color fitness and the spatial distance:

$$\beta(u_i^j, k_l^j) = \beta_c(u_i^j, k_l^j) + \omega \beta_s(u_i^j, k_l^j) \quad (8)$$

where ω is a weight parameter to trade off the color fitness and spatial distance. ω is assigned as 0.5 in our experiment. Generally a small β indicates that the labelled pixel has a close correlation with the unknown pixel, and they have a high probability of belonging to the same class.

Hierarchical Update: After performing initialization with the hierarchical strategy, in each hierarchy, the correlations between each unknown pixel and its neighboring labelled pixels (vessel pixels and background pixels) included in a 9×9 grid are computed. Then the labelled pixel with the closest correlation is chosen, and its label is assigned to the unknown pixel. After all unknown pixels in one hierarchy are updated, they are used for updating the next hierarchy. The unknown pixels are updated from the first hierarchy to the last hierarchy. An example to illustrate the process of updating unknown pixels in one hierarchy is shown in Fig.8.

C. Postprocessing

Since some non-vessel regions may still exist in the final segmented vessel image I_v , the regions whose $Area < a_2$ && $Extent > e_2$ && $VRatio < r$ in I_v are abandoned to remove these non-vessel regions.

IV. DATASETS AND EVALUATION METRICS

In this section, three publicly available datasets are introduced. These datasets have been extensively used by other scientists to develop their own methods. Then some commonly used evaluation metrics are presented, which are also utilized in our experiment to make a comparison between the proposed model with several other approaches.

A. Datasets

The proposed model is evaluated on three standard datasets: DRIVE [6], STARE [15] and CHASE_DB1 [37].

DRIVE¹ consists of 40 fundus images. These images are taken by a Canon camera at 45° field of view (FOV). Each image is of 584×565 pixels. The DRIVE dataset is separated into two sets: a training set and a test set each including 20 fundus images. The training set is marked by two observers; The test set is marked by two independent observers.

¹<http://www.isi.uu.nl/Research/Databases/DRIVE/>

TABLE II
COMPARISON BETWEEN THE PROPOSED MODEL AND OTHER METHODS

Test Datasets	DRIVE					STARE					System	
	Methods	Acc	AUC	Se	Sp	Time	Acc	AUC	Se	Sp		Time
Supervised Methods												
Staal <i>et.al</i> [6]	0.944	-	-	-	-	15min	0.952	-	-	-	15min	1.0 GHz, 1-GB RAM
Soares <i>et.al</i> [7]	0.946	-	-	-	-	~3min	0.948	-	-	-	~3min	2.17 GHz, 1-GB RAM
Lupascu <i>et.al</i> [8]	0.959	-	0.720	-	-	-	-	-	-	-	-	-
Marin <i>et.al</i> [9]	0.945	0.843	0.706	0.980	~90s	0.952	0.838	0.694	0.982	~90s	2.13 GHz, 2-GB RAM	
Roychowdhury <i>et.al</i> [10]	0.952	0.844	0.725	0.962	3.11s	0.951	0.873	0.772	0.973	6.7s	2.6 GHz, 2-GB RAM	
Liskowski <i>et.al</i> [11]	0.954	0.881	0.781	0.981	-	0.973	0.921	0.855	0.986	-	NVIDIA GTX Tian GPU	
Daniele <i>et.al</i> [12]	0.956	0.875	0.767	0.983	15.31s	0.972	0.896	0.806	0.986	23.2s	NVIDIA Tian XP GPU	
Unsupervised Methods												
Hoover <i>et.al</i> [15]	-	-	-	-	-	-	0.928	0.730	0.650	0.810	5min	Sun SPARCstation 20
Mendonca <i>et.al</i> [17]	0.945	0.855	0.734	0.976	2.5min	0.944	0.836	0.699	0.973	3min	3.2 GHz, 980-MB RAM	
Lam <i>et.al</i> [41]	-	-	-	-	-	-	0.947	-	-	-	8min	1.83 GHz, 2-GB RAM
Al-Diri <i>et.al</i> [19]	-	-	0.728	0.955	11min	-	-	0.752	0.968	-	-	1.2 GHz
Lam and Yan <i>et.al</i> [20]	0.947	-	-	-	13min	0.957	-	-	-	13min	1.83 GHz, 2-GB RAM	
Perez <i>et.al</i> [42]	0.925	0.806	0.644	0.967	~2min	0.926	0.857	0.769	0.944	~2min	Parallel Cluster	
Miri <i>et.al</i> [43]	0.943	0.846	0.715	0.976	~50s	-	-	-	-	-	3 GHz, 1-GB RAM	
Budai <i>et.al</i> [44]	0.957	0.816	0.644	0.987	-	0.938	0.781	0.580	0.982	-	2.3 GHz, 4-GB RAM	
Nguyen <i>et.al</i> [45]	0.941	-	-	-	2.5s	0.932	-	-	-	2.5s	2.4 GHz, 2-GB RAM	
Yitian <i>et.al</i> [21]	0.954	0.862	0.742	0.982	-	0.956	0.874	0.780	0.978	-	3.1 GHz, 8-GB RAM	
Annunziata <i>et.al</i> [46]	-	-	-	-	-	0.956	0.849	0.713	0.984	<25s	1.9 GHz, 6-GB RAM	
Orlando <i>et.al</i> [47]	-	0.879	0.790	0.968	-	-	0.871	0.768	0.974	-	2.9 GHz, 64-GB RAM	
Proposed	0.960	0.858	0.736	0.981	10.72s 6.25s	0.957	0.880	0.791	0.970	15.74s 9.66s	2.5 GHz, 4-GB RAM NVIDIA GTX Tian GPU	

STARE² consists of 20 fundus images. These images are taken by a TopCon camera at 35° FOV. Each image is of 605 × 700 pixels. The STARE dataset is marked by two independent observers.

CHASE_DB1³ consists of 28 fundus images acquired from multiethnic school children. These images are captured by a Nidek camera at 30° FOV. Each image is of 960 × 999 pixels. The CHASE_DB1 is marked by two independent observers.

For the DRIVE, STARE and CHASE_DB1 datasets, the manual segmentations of the first observer are used in this work, which is a common choice for these datasets [5], [11], [21], [46].

B. Evaluation Metrics

For vessel segmentation, each pixel is classified as vessels or background, thereby resulting in four events: two correct (true) classifications and two incorrect (false) classifications (as shown in Table III).

TABLE III
FOUR EVENTS OF VESSEL CLASSIFICATION

	Vessel present	Vessel absent
Vessel detected	True Positive (TP)	False Positive (FP)
Vessel not detected	False Negative (FN)	True Negative(TN)

To evaluate the performance of the vessel segmentation

algorithms, three commonly used metrics are applied.

$$Sensitivity = \frac{TP}{TP + FN}$$

$$Specificity = \frac{TN}{TN + FP}$$

$$Accuracy = \frac{TP + TN}{TP + TN + FP + FN}$$

Sensitivity (*Se*) and Specificity (*Sp*) reflect the algorithm's ability to detect vessel pixels and background pixels. Accuracy (*Acc*) is a global measure of classification performance combining both *Se* and *Sp*. The performance of the vessel segmentation method is also measured by the area under a receiver operating characteristic (*ROC*) curve (*AUC*). The conventional *AUC* is calculated from a number of operating points, and normally used to evaluate the balanced data classification problem. However, in practice the researchers need to select an operating point to compare their method with other methods. In addition blood vessel segmentation is an imbalanced classification problem, in which the number of vessel pixels is much smaller than the number of background pixels. In order to evaluate the performance of blood vessel segmentation properly, $AUC = (Se + Sp)/2$ [21], [48] is applied to indicate the overall vessel segmentation performance, which is suitable to describe the overall performance of imbalanced data classification problem and specifically for the case when only one operating point is used. The calculation time of extracting blood vessels from a fundus images is also stored.

In addition, the Dice scores (*D*) [21] is applied to evaluate the similarity between the manual segmentations and results of vessel segmentation algorithms: $D = 2(M \cap S)/(M + S)$,

²<http://www.ces.clemson.edu/~ahoover/stare/>

³<https://blogs.kingston.ac.uk/retinal/chasedb1/>

TABLE IV
THE SEGMENTATION PERFORMANCE OF THE PROPOSED MODEL ON THREE TEST DATASETS

Dataset	Method	Acc	AUC	Se	Sp	D	Time(s)
DRIVE	Trimap (Treating the unknown regions as background regions)	0.959	0.833	0.679	0.986	0.765	5.841
	The proposed hierarchical matting model without vessel skeleton extraction	0.960	0.837	0.688	0.986	0.771	11.959
	The proposed hierarchical matting model with vessel skeleton extraction	0.960	0.859	0.736	0.981	0.780	10.720
STARE	Trimap (Treating the unknown regions as background regions)	0.958	0.853	0.728	0.977	0.737	7.741
	The proposed hierarchical matting model without vessel skeleton extraction	0.959	0.862	0.748	0.976	0.745	16.563
	The proposed hierarchical matting model with vessel skeleton extraction	0.957	0.881	0.791	0.970	0.752	15.740
CHASE_DB1	Trimap (Treating the unknown regions as background regions)	0.948	0.771	0.565	0.977	0.598	21.088
	The proposed hierarchical matting model without vessel skeleton extraction	0.954	0.789	0.597	0.981	0.650	60.847
	The proposed hierarchical matting model with vessel skeleton extraction	0.951	0.815	0.657	0.973	0.665	50.710

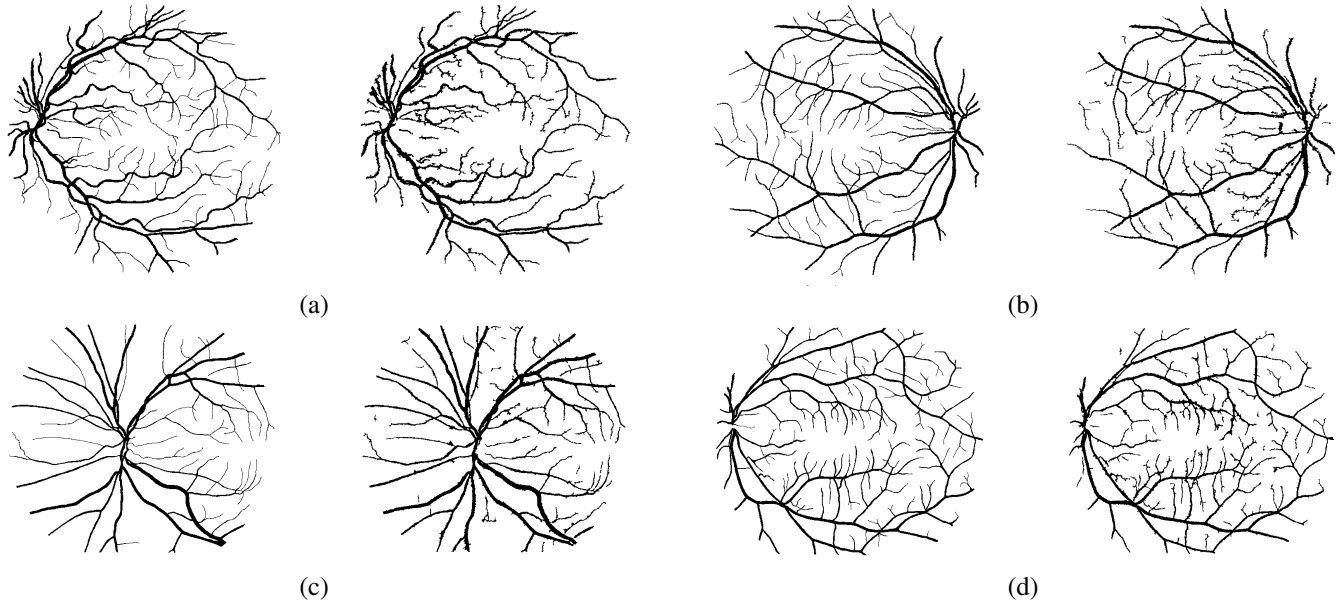


Fig. 9. Ground truth (left) and segmentation result (right): (a) and (b) are the images from DRIVE dataset, (c) and (d) are the images from the STARE dataset

where M represents the manual segmentation and S represents the segmentation result.

V. EXPERIMENTS AND RESULTS

In this section, four experiments are conducted to evaluate the proposed hierarchical image matting model. In the first experiment, the comparison between the proposed model and other state-of-art methods was presented. In the second experiment, the vessel segmentation performance of the proposed model was analyzed. In the third experiment, the proposed hierarchical image matting model was compared with several other conventional image matting models. In the last experiment, the sensitivity analysis of the threshold values of the region features and the weight parameter ω used in the work was given.

A. Comparison with other methods

In this section, the proposed model is compared with other methods on two most popular public datasets: DRIVE and STARE. The CHASE_DB1 dataset is not employed here since it is relatively new and has relatively few results in the literature. The segmentation performance and calculation time

of the proposed model in comparison with other methods on the DRIVE and STARE datasets are given in Table II. The Dice scores is not introduced in Table II since it is not given by other methods. For the DRIVE dataset, the accuracy of the proposed model is the highest among all existing methods with $Acc = 0.960$, $Se = 0.736$ and $Sp = 0.981$. On the STARE dataset, the accuracy and AUC of the proposed model are the highest among unsupervised methods with $Acc = 0.957$, $AUC = 0.880$. In addition, the proposed model has a low calculation time compared with other segmentation methods. Although the supervised method [11] has the best performance on STARE dataset, the method is computationally more complex due to the use of deep neural networks, which may need retraining for new datasets. The supervised method [12] obtains excellent segmentation results on DRIVE and STARE datasets, and has a low computational time with a powerful system. However, it may need retraining for new datasets. And the proposed method has a lower calculation time.

TABLE V
SEGMENTATION PERFORMANCE OF EIGHT DIFFERENT IMAGE MATTING MODELS AND THE PROPOSED MODEL

Dataset	Metrics	Anat Model	Zheng Model	Shahrian Model	Improving Model	Karacan Model	Cho Model	Li Model	Aksoy Model	Proposed
DRIVE	Acc	0.958	0.958	0.921	0.958	0.958	0.959	0.958	0.958	0.960
	AUC	0.862	0.862	0.903	0.862	0.862	0.859	0.860	0.862	0.859
	Se	0.746	0.746	0.881	0.746	0.746	0.738	0.741	0.746	0.736
	Sp	0.978	0.978	0.925	0.978	0.978	0.980	0.979	0.978	0.981
	D	0.774	0.774	0.656	0.774	0.774	0.777	0.774	0.774	0.780
	Time(s)	10.036	11.837	120.552	360.000	482.569	118.057	80.905	41.407	10.720
STARE	Acc	0.944	0.954	0.912	0.954	0.954	0.954	0.955	0.954	0.957
	AUC	0.839	0.883	0.906	0.883	0.883	0.884	0.882	0.883	0.881
	Se	0.714	0.799	0.899	0.799	0.799	0.802	0.796	0.800	0.791
	Sp	0.964	0.966	0.913	0.966	0.966	0.966	0.967	0.966	0.970
	D	0.690	0.744	0.638	0.744	0.744	0.745	0.745	0.744	0.752
	Time(s)	11.376	14.185	145.860	381.923	563.494	95.968	93.143	43.221	15.740
CHASE_DB1	Acc	0.944	0.944	0.918	0.944	0.944	0.944	0.945	0.944	0.951
	AUC	0.820	0.820	0.858	0.820	0.815	0.823	0.819	0.817	0.815
	Se	0.675	0.675	0.790	0.675	0.676	0.682	0.673	0.668	0.657
	Sp	0.964	0.964	0.927	0.965	0.954	0.964	0.965	0.965	0.973
	D	0.641	0.641	0.588	0.641	0.641	0.644	0.642	0.638	0.665
	Time(s)	29.047	40.587	340.899	797.960	2710.425	225.102	238.169	114.782	50.710

B. Vessel Segmentation Performance

The segmentation performance of the proposed method on three public available datasets is given in Table IV. Fig.9 presents Some exemplary segmentation results.

When treating the unknown regions as background regions, trimap can achieve segmentation results of $Acc = 0.959$, $AUC = 0.833$, $Se = 0.679$, $Sp = 0.986$, $D = 0.765$ on the DRIVE dataset, $Acc = 0.958$, $AUC = 0.853$, $Se = 0.728$, $Sp = 0.977$, $D = 0.737$ on the STARE dataset, $Acc = 0.948$, $AUC = 0.771$, $Se = 0.565$, $Sp = 0.977$, $D = 0.598$ on the CHASE_DB1 dataset, respectively. These segmentation performances show that trimap can already have fairly good segmentation performance, which indicates that the selection of region features is effective in segmenting blood vessels.

However, the performance is still not satisfactory enough when compared with other methods. A hierarchical image matting model is proposed to improve the segmentation performance. $AUC = 0.837, 0.862, 0.789$ achieved by the proposed hierarchical matting model on the DRIVE, STARE and CHASE_DB1 are 0.4%, 0.9% and 1.8% higher than that of trimap, respectively. $Se = 0.688, 0.748, 0.597$ achieved by the proposed hierarchical matting model on the DRIVE, STARE and CHASE_DB1 are 0.9%, 2% and 2.8% higher than that of trimap, respectively. In addition, $D = 0.771, 0.745, 0.650$ obtained by the proposed hierarchical matting model on the DRIVE, STARE and CHASE_DB1 are 0.6%, 0.8% and 5.2% higher than that of trimap, respectively.

The segmentation performance can be further improved by applying vessel skeleton extraction. From Table IV, it can be observed that compared with the proposed image matting model without vessel skeleton extraction, the matting model with vessel skeleton extraction can achieve 4.8% increase of *Sensitivity*, 2.2% increase of *AUC* and 0.9% increase of *D* on the DRIVE dataset, 4.3% increase of *Sensitivity*, 1.9% increase of *AUC* and 0.7% increase of *D* on the STARE dataset, 6% increase of *Sensitivity*, 2.8% increase of *AUC* and 1.5% increase of *D* on the CHASE_DB1 dataset, which demonstrates the effectiveness of applying the mechanism of vessel skeleton extraction.

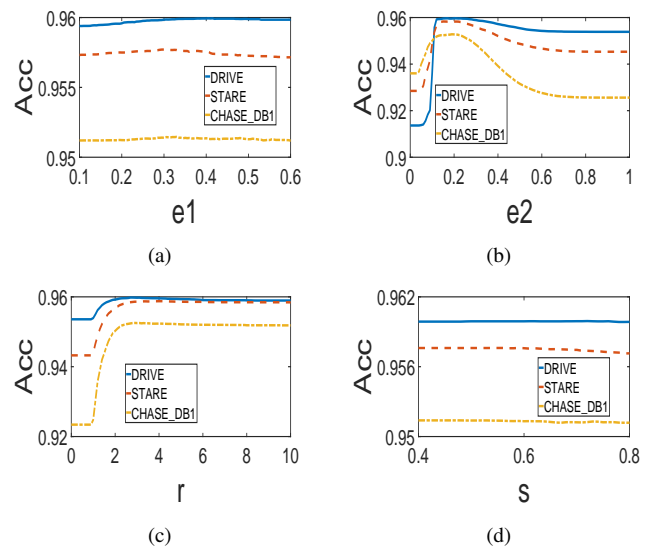


Fig. 10. Sensitivity analysis of threshold values of region features used in the work. (a) Variations in mean segmentation accuracy by varying e_1 when $r = 2.2$, $s = 0.53$, $e_2 = 0.25$. (b) Variations in mean segmentation accuracy by varying e_2 when $r = 2.2$, $e_1 = 0.35$, $s = 0.53$. (c) Variations in mean segmentation accuracy by varying r when $e_1 = 0.35$, $s = 0.53$, $e_2 = 0.25$. (d) Variations in mean segmentation accuracy by varying s when $r = 2.2$, $e_1 = 0.35$, $e_2 = 0.25$.

C. Comparison with image matting models

The effectiveness of the proposed model in blood vessel segmentation has been validated through previous experiments. In order to further verify the effectiveness of our model, the proposed model is compared with eight other state-of-art image matting models: Anat Model [26], Zheng Model [22], Shahrian Model [28], Improving Model [29], Karacan Model [31], Cho Model [32], Li Model [33] and Aksoy Model [34]. The segmentation results of these models on the DRIVE, STARE, and CHASE_DB1 datasets are given in Table V. The proposed model outperforms these image matting models in terms of *Acc* and *Sp* in the DRIVE, STARE and CHASE_DB1 datasets.

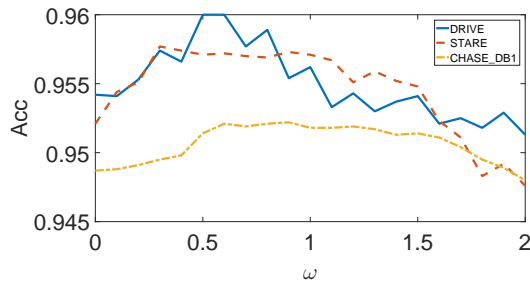


Fig. 11. Variations in mean segmentation accuracy by varying ω .

D. Sensitivity analysis of threshold values of region features and the weight parameter

The default threshold values of region features: $e_1 = 0.35$, $r = 2.2$, $s = 0.53$, $e_2 = 0.25$ are applied in this experiment. To demonstrate the insensitivity of the proposed model to these threshold values, the variations in Acc by varying e_1 , e_2 , r and s are given in Fig.10.(a), (b), (c) and (d). From Fig.10, it can be observed that the proposed model can maintain high segmentation accuracy on the DRIVE, STARE and CHASE_DB1 datasets as e_1 varies in $[0.2, 0.6]$ or e_2 varies in $[0.15, 0.3]$; For r and s , the proposed model can maintain high segmentation accuracy as r varies in $[2, 10]$ or s varies in $[0.4, 0.8]$. In addition, the variation in Acc by varying ω is given in Fig.11. From Fig.11, it can be observed that the proposed model can maintain high segmentation accuracy on the DRIVE, STARE and CHASE_DB1 datasets as ω varies in $[0.4, 0.8]$. From the above observation, it can be seen that the proposed model is not sensitive to these threshold values of region features and the weight parameter ω .

VI. CONCLUSION

Image matting means precisely segmenting the foreground from an image, which is crucial in many important applications. However, to the best of our knowledge, image matting has rarely been employed previously to extract blood vessels from fundus image. The major reason may be that generating a user specified trimap for vessel segmentation is an extremely laborious and time-consuming task. In addition, a proper image matting model needs to be designed carefully to improve the vessel segmentation performance. In order to address these issues, region features of blood vessels are first employed to generate the trimap automatically. Then a hierarchical image matting model is proposed to extract the vessel pixels from the unknown regions. More specifically, a hierarchical strategy is integrated into the image matting model for blood vessel segmentation.

The proposed model is very efficient and effective in blood vessel segmentation, which achieves a segmentation accuracy of 96.0%, 95.7% and 95.1% on three public available datasets with an average time of 10.72s, 15.74s and 50.71s, respectively. The experimental results show that it is a very competitive model compared with many other segmentation approaches.

ACKNOWLEDGMENT

This research work was supported by Guangdong Key Laboratory of Digital Signal and Image Processing, the National Natural Science Foundation of China under Grant (61175073, 61300159, 61332002, 51375287), the Natural Science Foundation of Jiangsu Province of China under grant SBK2018022017.

REFERENCES

- [1] S. Abbasi-Sureshjani, M. Favali, G. Citti, A. Sarti, and B. M. T. H. Romeny, "Curvature integration in a 5d kernel for extracting vessel connections in retinal images," *IEEE Transactions on Image Processing*, vol. PP, no. 99, pp. 1–1, 2017.
- [2] J. J. Kanski and B. Bowling, *Clinical Ophthalmology: A Systematic Approach*. Elsevier Health Sciences, 2011.
- [3] M. W. Law and A. C. Chung, "Segmentation of intracranial vessels and aneurysms in phase contrast magnetic resonance angiography using multirange filters and local variances," *IEEE Transactions on image processing*, vol. 22, no. 3, pp. 845–859, 2013.
- [4] Y. Cheng, X. Hu, J. Wang, Y. Wang, and S. Tamura, "Accurate vessel segmentation with constrained b-snake," *IEEE Transactions on Image Processing*, vol. 24, no. 8, pp. 2440–2455, 2015.
- [5] M. M. Fraz, P. Remagnino, A. Hoppe, B. Uyyanonvara, A. R. Rudnicka, C. G. Owen, and S. A. Barman, "Blood vessel segmentation methodologies in retinal images—a survey," *Computer Methods and Programs In Biomedicine*, vol. 108, no. 1, pp. 407–433, 2012.
- [6] J. Staal, M. D. Abràmoff, M. Niemeijer, M. A. Viergever, and B. van Ginneken, "Ridge-based vessel segmentation in color images of the retina," *IEEE Transactions on Medical Imaging*, vol. 23, no. 4, pp. 501–509, 2004.
- [7] J. V. Soares, J. J. Leandro, R. M. Cesar, H. F. Jelinek, and M. J. Cree, "Retinal vessel segmentation using the 2-d gabor wavelet and supervised classification," *IEEE Transactions on Medical Imaging*, vol. 25, no. 9, pp. 1214–1222, 2006.
- [8] C. A. Lupascu, D. Tegolo, and E. Trucco, "Fabc: Retinal vessel segmentation using adaboost," *IEEE Transactions on Information Technology in Biomedicine*, vol. 14, no. 5, pp. 1267–1274, 2010.
- [9] D. Marín, A. Aquino, M. E. Gegúndez-Arias, and J. M. Bravo, "A new supervised method for blood vessel segmentation in retinal images by using gray-level and moment invariants-based features," *IEEE Transactions on Medical Imaging*, vol. 30, no. 1, pp. 146–158, 2011.
- [10] S. Roychowdhury, D. D. Koozekanani, and K. K. Parhi, "Blood vessel segmentation of fundus images by major vessel extraction and subimage classification," *IEEE Journal of Biomedical and Health Informatics*, vol. 19, no. 3, pp. 1118–1128, 2015.
- [11] P. Liskowski and K. Krawiec, "Segmenting retinal blood vessels with deep neural networks," *IEEE Transactions on Medical Imaging*, vol. 35, pp. 1–1, 2016.
- [12] O. S. Daniele Cortinovia, "Retina blood vessel segmentation with a convolution neural network (u-net)," available: <https://github.com/orobix/retina-unet>, 2016.
- [13] O. Ronneberger, P. Fischer, and T. Brox, "U-net: Convolutional networks for biomedical image segmentation," in *International Conference on Medical image computing and computer-assisted intervention*. Springer, 2015, pp. 234–241.
- [14] A. F. Frangi, W. J. Niessen, K. L. Vincken, and M. A. Viergever, "Multiscale vessel enhancement filtering," in *International Conference on Medical Image Computing and Computer-Assisted Intervention*. Springer, 1998, pp. 130–137.
- [15] A. Hoover, V. Kouznetsova, and M. Goldbaum, "Locating blood vessels in retinal images by piecewise threshold probing of a matched filter response," *IEEE Transactions on Medical Imaging*, vol. 19, no. 3, pp. 203–210, 2000.
- [16] F. K. Quek and C. Kirbas, "Vessel extraction in medical images by wave-propagation and traceback," *IEEE Transactions on Medical Imaging*, vol. 20, no. 2, pp. 117–131, 2001.
- [17] A. M. Mendonca and A. Campilho, "Segmentation of retinal blood vessels by combining the detection of centerlines and morphological reconstruction," *IEEE Transactions on Medical Imaging*, vol. 25, no. 9, pp. 1200–1213, 2006.
- [18] K. Sum and P. Y. Cheung, "Vessel extraction under non-uniform illumination: A level set approach," *IEEE Transactions on Biomedical Engineering*, vol. 55, no. 1, pp. 358–360, 2008.

- [19] B. Al-Diri, A. Hunter, and D. Steel, "An active contour model for segmenting and measuring retinal vessels," *IEEE Transactions on Medical Imaging*, vol. 28, no. 9, pp. 1488–1497, 2009.
- [20] B. S. Lam, Y. Gao, and A. W.-C. Liew, "General retinal vessel segmentation using regularization-based multiconcavity modeling," *IEEE Transactions on Medical Imaging*, vol. 29, no. 7, pp. 1369–1381, 2010.
- [21] Y. Zhao, L. Rada, K. Chen, S. P. Harding, and Y. Zheng, "Automated vessel segmentation using infinite perimeter active contour model with hybrid region information with application to retinal images," *IEEE Transactions on Medical Imaging*, vol. 34, no. 9, pp. 1797–1807, 2015.
- [22] Y. Zheng and C. Kambhamettu, "Learning based digital matting," in *Computer Vision and Pattern Recognition (CVPR), 2009 IEEE Conference on*. IEEE, 2009, pp. 889–896.
- [23] P. Talwar and M. D. Gupta, "Alpha-matting based retinal vessel extraction," Jun. 13 2017, US Patent 9,675,247.
- [24] Q. Chen, D. Li, and C. Tang, "Knn matting," in *Computer Vision and Pattern Recognition (CVPR), 2012 IEEE Conference on*, 2012, pp. 869–876.
- [25] Y.-Y. Chuang, B. Curless, D. H. Salesin, and R. Szeliski, "A bayesian approach to digital matting," in *Computer Vision and Pattern Recognition (CVPR), 2001 IEEE Conference on*, vol. 2. IEEE, 2001, pp. II–II.
- [26] A. Levin, D. Lischinski, and Y. Weiss, "A closed-form solution to natural image matting," *IEEE Transactions on Pattern Analysis and Machine Intelligence*, vol. 30, no. 2, pp. 228–242, 2008.
- [27] K. He, J. Sun, and X. Tang, "Fast matting using large kernel matting laplacian matrices," in *Computer Vision and Pattern Recognition (CVPR), 2010 IEEE Conference on*. IEEE, 2010, pp. 2165–2172.
- [28] E. Shahrian and D. Rajan, "Weighted color and texture sample selection for image matting," *IEEE Transactions on Image Processing*, vol. 22, no. 11, pp. 4260–4270, 2013.
- [29] E. Shahrian, D. Rajan, B. Price, and S. Cohen, "Improving image matting using comprehensive sampling sets," in *Computer Vision and Pattern Recognition (CVPR), 2013 IEEE Conference on*, 2013, pp. 636–643.
- [30] D. Cho, S. Kim, and Y.-W. Tai, "Consistent matting for light field images," in *European Conference on Computer Vision*. Springer, 2014, pp. 90–104.
- [31] L. Karacan, A. Erdem, and E. Erdem, "Image matting with kl-divergence based sparse sampling," in *Computer Vision and Pattern Recognition (CVPR), 2015 IEEE Conference on*, 2015, pp. 424–432.
- [32] D. Cho, Y.-W. Tai, and I. Kweon, "Natural image matting using deep convolutional neural networks," in *European Conference on Computer Vision*. Springer, 2016, pp. 626–643.
- [33] C. Li, P. Wang, X. Zhu, and H. Pi, "Three-layer graph framework with the sumd feature for alpha matting," *Computer Vision and Image Understanding*, vol. 162, pp. 34–45, 2017.
- [34] Y. Aksoy, T. O. Aydin, and M. Pollefeys, "Designing effective inter-pixel information flow for natural image matting," in *Computer Vision and Pattern Recognition (CVPR), 2017 IEEE Conference on*, 2017, pp. 228–236.
- [35] Y. Lee and S. Yang, "Parallel block sequential closed-form matting with fan-shaped partitions," *IEEE Transactions on Image Processing*, vol. 27, no. 2, pp. 594–605, 2018.
- [36] Z. Fan, J. Lu, and Y. Rong, "Automated blood vessel segmentation of fundus images using region features of vessels," in *Computational Intelligence (SSCI), 2016 IEEE Symposium Series on*. IEEE, 2016, pp. 1–6.
- [37] M. M. Fraz, P. Remagnino, A. Hoppe, B. Uyyanonvara, A. R. Rudnicka, C. G. Owen, and S. A. Barman, "An ensemble classification-based approach applied to retinal blood vessel segmentation," *IEEE Transactions on Biomedical Engineering*, vol. 59, no. 9, pp. 2538–2548, 2012.
- [38] J. Wang and M. F. Cohen, "An iterative optimization approach for unified image segmentation and matting," in *Tenth IEEE International Conference on Computer Vision (ICCV'05) Volume 1*, vol. 2. IEEE, 2005, pp. 936–943.
- [39] P. Bankhead, C. N. Scholfield, J. G. McGeown, and T. M. Curtis, "Fast retinal vessel detection and measurement using wavelets and edge location refinement," *PloS One*, vol. 7, no. 3, p. e32435, 2012.
- [40] R. Kresch and D. Malah, "Skeleton-based morphological coding of binary images," *IEEE Transactions on Image Processing*, vol. 7, no. 10, pp. 1387–1399, 1998.
- [41] B. S. Y. Lam and H. Yan, "A novel vessel segmentation algorithm for pathological retina images based on the divergence of vector fields," *IEEE Transactions on Medical Imaging*, vol. 27, no. 2, pp. 237–246, 2008.
- [42] M. A. Palomera-Pérez, M. E. Martínez-Pérez, H. Benítez-Pérez, and J. L. Ortega-Arjona, "Parallel multiscale feature extraction and region growing: Application in retinal blood vessel detection," *IEEE Transactions on Information Technology in Biomedicine*, vol. 14, no. 2, pp. 500–506, 2010.
- [43] M. S. Miri and A. Mahloojifar, "Retinal image analysis using curvelet transform and multistructure elements morphology by reconstruction," *IEEE Transactions on Biomedical Engineering*, vol. 58, no. 5, pp. 1183–1192, 2011.
- [44] I. Section, "Robust vessel segmentation in fundus images," *International Journal of Biomedical Imaging*, vol. 2013, no. 6, p. 154860, 2013.
- [45] U. T. Nguyen, A. Bhuiyan, L. A. Park, and K. Ramamohanarao, "An effective retinal blood vessel segmentation method using multi-scale line detection," *Pattern Recognition*, vol. 46, no. 3, pp. 703–715, 2013.
- [46] R. Annunziata, A. Garzelli, L. Ballerini, A. Mecocci, and E. Trucco, "Leveraging multiscale hessian-based enhancement with a novel exudate inpainting technique for retinal vessel segmentation," *IEEE Journal of Biomedical and Health Informatics*, vol. 20, no. 4, pp. 1129–1138, 2016.
- [47] J. I. Orlando, E. Prokofyeva, and M. B. Blaschko, "A discriminatively trained fully connected conditional random field model for blood vessel segmentation in fundus images," *IEEE Transactions on Biomedical Engineering*, vol. 64, no. 1, pp. 16–27, 2017.
- [48] X. Hong, S. Chen, and C. J. Harris, "A kernel-based two-class classifier for imbalanced data sets," *IEEE Transactions on Neural Networks*, vol. 18, no. 1, pp. 28–41, 2007.



Zhun Fan received the B.S. and M.S. degrees in control engineering from Huazhong University of Science and Technology, Wuhan, China, in 1995 and 2000, respectively, and the Ph.D. degree in electrical and computer engineering from the Michigan State University, Lansing, MI, USA, in 2004. He is currently a Full Professor with Shantou University (STU), Shantou, China. He also serves as the Head of the Department of Electrical Engineering and the Director of the Guangdong Provincial Key Laboratory of Digital Signal and Image Processing. Before joining STU, he was an Associate Professor with the Technical University of Denmark (DTU) from 2007 to 2011, first with the Department of Mechanical Engineering, then with the Department of Management Engineering, and as an Assistant Professor with the Department of Mechanical Engineering in the same university from 2004 to 2007. He has been a Principle Investigator of a number of projects from Danish Research Agency of Science Technology and Innovation and National Natural Science Foundation of China. His research is also supported by the National Science Foundation. His major research interests include intelligent control and robotic systems, robot vision and cognition, MEMS, computational intelligence, design automation, optimization of mechatronic systems, machine learning and image processing.



Jiewei Lu is with the key lab of digital signal and image processing of Guangdong Province, Shantou University, Shantou, China, where he is currently pursuing the M.S. degree in information and communication with the School of Engineering. His current research interests include medical image analysis, image processing and machine learning.



Caimin Wei received the B.S. degree in mathematics and applied mathematics from GuangXi University for Nationalities, Guangxi, China, in 2000, the M.Sc. degree in operational research and cybernetics from Yanshan University, Hebei, China, in 2002 and the Ph.D. degree in operational research and cybernetics from Dalian University of Technology, Dalian, China, in 2005. He is currently a Full Professor with the Department of Mathematics, Shantou University (STU), Shantou, China. His current research interests include queuing theory, scheduling theory and

financial mathematics.



Han Huang received the B.Man. degree in applied mathematics and the Ph.D. degree in computer science from the South China University of Technology (SCUT), Guangzhou, China, in 2002 and 2008, respectively. He is currently a Professor with the School of Software Engineering, SCUT. He is also the Director of Intelligent Algorithm and Intelligent Software Studio. His current research interests include evolutionary computation, swarm intelligence, and their application.

Dr. Huang is a Senior Member of CCF.



Xinye Cai received the B.Sc. degree in information engineering from the Huazhong University of Science and Technology, Wuhan, China, in 2004, the M.Sc. degree in electronic engineering from the University of York, York, U.K., in 2006, and the Ph.D. degree in electrical engineering from Kansas State University, Manhattan, KS, USA, in 2009. He is an Associate Professor with the Department of Computer Science and Technology, Nanjing University of Aeronautics and Astronautics, Nanjing, China, where he is currently leading an Intelligent

Optimization Research Group. His current research interests include evolutionary computation, optimization, and data mining and their applications.

Dr. Cai was the winner of the Evolutionary Many-Objective Optimization Competition at the 2017 IEEE Congress on Evolutionary Computation. He serves as Associate Editor for the Swarm and Evolutionary Computation.



Xinjian Chen received the Ph.D. degree in pattern recognition and machine intelligence from the Institute of Automation, Chinese Academy of Sciences, Beijing, China, in 2006. He is a Distinguished Professor with the School of Electrical and Information Engineering, Soochow University, Suzhou, China, and the Director of Medical Image Processing, Analysis and Visualization Laboratory. He has authored or coauthored more than 100 papers in prestigious journals and conferences, including

IEEE TRANSACTIONS ON MEDICAL IMAGING, IEEE TRANSACTIONS ON BIOMEDICAL ENGINEERING, etc. His research interests include medical image processing and analysis, pattern recognition, and machine learning.

Dr. Chen has served as Associate Editor for the IEEE TRANSACTIONS ON MEDICAL IMAGING and the IEEE JOURNAL OF TRANSLATIONAL ENGINEERING IN HEALTH AND MEDICINE.